In situ ammonium formation mediates efficient hydrogen production from natural seawater splitting

Xiao-Long Zhang [1,3], Peng-Cheng Yu[1,3], Shu-Ping Sun[1,3], Lei Shi[1], Peng-Peng Yang [1], Zhi-Zheng Wu [1], Li-Ping Chi [1], Ya-Rong Zheng [2] ✉ & Min-Rui Gao [1] ✉

Seawater electrolysis using renewable electricity offers an attractive route to sustainable hydrogen production, but the sluggish electrode kinetics and poor durability are two major challenges. We report a molybdenum nitride (Mo_2N) catalyst for the hydrogen evolution reaction with activity comparable to commercial platinum on carbon (Pt/C) catalyst in natural seawater. The catalyst operates more than 1000 hours of continuous testing at $100\,mA\,cm^{-2}$ without degradation, whereas massive precipitate (mainly magnesium hydroxide) forms on the Pt/C counterpart after 36 hours of operation at $10\,mA\,cm^{-2}$. Our investigation reveals that ammonium groups generate in situ at the catalyst surface, which not only improve the connectivity of hydrogen-bond networks but also suppress the local pH increase, enabling the enhanced performances. Moreover, a zero-gap membrane flow electrolyser assembled by this catalyst exhibits a current density of $1\,A\,cm^{-2}$ at 1.87 V and 60 °C in simulated seawater and runs steadily over 900 hours.

Water electrolysis is the most promising green hydrogen technology that uses renewable electricity to produce H_2 fuel without carbon emissions[1]. Current low-temperature water electrolysis devices, including alkaline electrolyser and proton exchange membrane (PEM) electrolyser, rely on high-purity water feeds[2,3]; this, however, will raise severe issue of freshwater resource shortage when large-scale commercialization of these devices becomes prevalent[4]. Direct seawater splitting is potentially an ideal solution to this issue, as the oceans account for 96.5% of the water reserves on Earth[5,6]. However, the complex components of natural seawater possess manifold challenges with respect to the efficiency and durability of this technology[4,6,7], including (i) dramatic pH fluctuations nearby the electrode surfaces, (ii) physical blockages at the cathode due to the formation of insoluble precipitates and (iii) competitive reactions between the oxygen evolution reaction (OER) and chloride electro-oxidation chemistry at the anode.

Over the past years, the majority of research efforts have centered on avoiding the unwanted chloride oxidations on the anode side, and an important progress has been achieved[8–10]. By contrast, less attention has been given to the salt deposition issue at the cathode that causes active site blocking and corrosion. Despite natural seawater is approximately neutral (pH ~7.5–8.4)[11], the local pH in the vicinity of cathode increases greatly during electrolysis, resulting in precipitation of seawater cations (mainly Mg^{2+} and Ca^{2+}) in the form of hydroxides[6,12]. Indirect electrolysis of seawater coupled with external pre-desalination and purification processes can remove major seawater ions, but this approach needs additional energy input, rendering it less cost effective[13]. Introducing chemical additives, such as KOH (US$800 per tonne)[7], into seawater could allow these cations to precipitate out via hydroxide formation, which is then filtered before electrolysis[14,15]. However, this greatly complicates the electrolysis process and adds the cost issue. A recently developed membrane-based seawater

[1]Division of Nanomaterials & Chemistry, Hefei National Laboratory for Physical Sciences at the Microscale, University of Science and Technology of China, Hefei, China. [2]School of Chemistry and Chemical Engineering, Anhui Province Key Laboratory of Value-Added Catalytic Conversion and Reaction Engineering, Anhui Province Engineering Research Center of Flexible and Intelligent Materials, Hefei University of Technology, Hefei, Anhui, China. [3]These authors contributed equally: Xiao-Long Zhang, Peng-Cheng Yu, Shu-Ping Sun. ✉e-mail: yrzh@hfut.edu.cn; mgao@ustc.edu.cn

electrolyser has enabled 100% ion-blocking efficiency via an in situ self-driven water purification design[16]. The approach, although side-reaction-free and corrosion-free, requires 2.25 V to reach a current density of 0.4 A cm⁻². This performance was comparable to alkalized seawater electrolysers with metrics of >2 V to achieve 0.4 A cm⁻² to 0.7 A cm⁻² (23–80 °C)[17–19], while remaining inferior to that of PEM freshwater electrolysers those can attain 1 A cm⁻² at 1.55 V to 2.1 V (80 °C)[20–22].

In addition, compared with alkalized water, the kinetics of both anodic OER and cathodic hydrogen evolution reaction (HER) become sluggish under neutral seawater environments, which requires larger overpotentials to attain desired current densities and therefore reduces the overall electrolysis efficiency[23–25]. Herein, we address these challenges using a molybdenum nitride (Mo_2N) catalyst that synthesized via a simple and rapid nitrogen plasma irradiation method. During natural seawater electrolysis, we find that ammonium (NH_4^+) cations generate in situ on the catalyst surface, which can be hydrogen-bonded with hydroxyl (OH^-) groups from the interfacial H_2O dissociation and consequently prevents the hydroxide formation. Meanwhile, these NH_4^+ groups also greatly improve the connectivity of hydrogen-bond networks in the electric double layer (EDL), lowering the hydrogen transfer barrier and enhancing the HER energetics. As a result, the catalyst demonstrates enhanced activity and long-term stability as the cathode in a seawater electrolyser.

Results

Preparation of metal nitride catalysts

Transition metal nitrides (TMNs) are a family of functional materials that synergize the properties of high electrical conductivity, good electrochemical stability, and corrosion resistance and are used widely for electrolysis[26,27]. Recently, we reported that nickel nitride (Ni_3N) and zirconium nitride (ZrN) were applied as high-performance electrocatalysts for hydrogen oxidation and oxygen reduction, respectively, in a fuel cell[28]. We reasoned that the unique features of TMNs would offer catalysts that can survive the harsh conditions encountered in seawater. To examine the potential, we prepared a series of TMNs, including ScN, TiN, Ni_3N, YN, ZrN, Mo_2N, and InN, by means of plasma-enhanced chemical vapor deposition (PECVD). This synthetic method enables ionization of N_2 to generate energetic nitrogen plasmas, which can substantially enhance the reactivity between nitrogen and metal precursors, yielding high-purity TMNs[29] (see Methods; Supplementary Fig. 1; Supplementary Table 1). Taken Mo_2N as an example, the X-ray diffraction (XRD) patterns (Fig. 1a) showed that the metallic Mo precursor was successfully converted into Mo_2N phase. Scanning transmission electron microscopy (STEM) image and STEM with energy-dispersive spectroscopy (STEM-EDS) element maps exhibited particulate morphology of Mo_2N with homogeneous distribution of Mo and N (Fig. 1b and Supplementary Fig. 2a, b). High-resolution transmission electron microscope (HRTEM) image (Fig. 1c) depicted continuous lattice fringes with a spacing of 0.24 nm, corresponding to Mo_2N (11-1) planes. The N 1s X-ray photoelectron spectroscopy (XPS) (Supplementary Fig. 2c) and the Mo K-edge extended X-ray absorption fine structure (EXAFS) (Supplementary Figs. 2d, e and Supplementary Table 2) analyses both revealed Mo-N bond in the sample. Raman spectroscopy measurements (Supplementary Fig. 2f) showed that a broad band <350 cm⁻¹ arose from the Mo precursor after nitrogen plasma irradiation, which are in good agreement with previous report of Raman modes of Mo_2N[30,31]. Besides Mo_2N, the evidences of obtaining other pure TMNs, i.e., ScN, TiN, Ni_3N, YN, ZrN, and InN, are presented in Supplementary Figs. 3–8 and Supplementary Table 3.

Electrocatalytic performance in natural seawater

We assessed the HER activity of these TMN catalysts using the rotating disk electrode (RDE) method in real seawater (pH 7.84 ± 0.02; Gulf of Mexico, Alabama, USA). As a benchmark, commercial Pt/C catalyst (20

weight % Pt on Vulcan XC72R carbon) was also examined. Inductively coupled plasma atomic emission spectrometry (ICP-AES) analysis showed that the seawater Mg^{2+} and Ca^{2+} concentrations were about 49.12 and 9.90 mmol L⁻¹ (Fig. 1d; Supplementary Table 4), respectively. Such high concentrations of the two harmful seawater cations would cause massive precipitations of $Mg(OH)_2$ and $Ca(OH)_2$, blocking the catalytic active sites. We screened all above TMN catalysts for HER and found that Mo_2N shows the optimal activity (Supplementary Fig. 9). For example, the Mo_2N catalyst required an overpotential of mere 311 ± 3 mV at 10 mA cm⁻² (Fig. 1e and Supplementary Figs. 10 and 11). The potential is considerably smaller than that of 806 ± 9 mV for commercial Mo catalyst and approaches that of 294 ± 4 mV for the Pt/C benchmark. The trend agrees well with our electrochemically active surface area (ECSA)-normalized HER polarizations (Supplementary Figs. 12 and 13). This result put Mo_2N among the most active non-precious metal catalysts documented in the aqueous high-salinity electrolytes (Supplementary Table 5). In situ Raman measurements show no sign of surface oxidation of Mo_2N during the HER (Supplementary Fig. 14). The H_2 evolved from seawater over Mo_2N was detected and quantified by gas chromatography (GC) at 10 mA cm⁻², which yielded a Faradaic efficiency of 99.9%, comparable to that of ~100% over Pt/C reference (Supplementary Fig. 15).

We also performed accelerated stability tests through potential cycling between −0.2 V to −0.4 V versus reversible hydrogen electrode (RHE) at 200 mV s⁻¹ in Ar-saturated natural seawater. As Fig. 1e shows, the Pt/C catalyst underwent an enormous degradation after potential cycles. The degradation is expected, owing to the hydroxide formation that blocked Pt sites. However, we were surprised to observe that Mo_2N subjected to the same aging measurement can largely retain its activity (Fig. 1e). Figure 1f shows that only 14-mV additional overpotential was required to reach 10 mA cm⁻² over Mo_2N catalyst after 50,000 potential cycles. By stark contrast, the Pt/C catalyst resulted in a 478-mV overpotential penalty at 10 mA cm⁻² after 10,000 cycles, which further climbed to 1098 mV after 50,000 cycles. Moreover, electrochemical impedance spectroscopy (EIS) measurements (Fig. 1g) revealed that the charge transfer resistance (R_{ct}) increases slightly (~4.57 Ohm) over Mo_2N after 50,000 cycles, whereas a significant R_{ct} increase by 2.3 kOhm was found over Pt/C under the same condition, suggesting constrained electron transfer from Pt/C surface to the reactant caused by hydroxide precipitates.

The Mo_2N catalyst was further subjected to a galvanostatic stability test at 100 mA cm⁻² (Fig. 1h). Continuous operation over 1000 hours was demonstrated with no clear sign of catalyst deactivation in seawater. This observation was in marked comparison to that of Pt/C catalyst, which showed fast deterioration in performance even holding the electrode at 10 mA cm⁻². After chronopotentiometry experiment, the morphology, composition and electronic states of Mo_2N were well maintained (Supplementary Figs. 16 and 17). We also compare the performance metrics of the Mo_2N catalyst with those reported previously in terms of overpotential at 10 mA cm⁻² and operating lifetime. The metrics obtained on Mo_2N outperform previous noble and non-noble catalysts those assessed under similar conditions (Supplementary Table 5).

Mechanistic investigation

To elucidate the source of high HER activity and, in particular, the unexpected stability, the real-time surface microenvironment and chemistry of Mo_2N and other reference catalysts were investigated in detail by in situ surface-enhanced infrared adsorption spectroscopy (SEIRAS) (Supplementary Fig. 18). In previous research, Chen and co-workers, through a combination of computational simulation and in situ SEIRAS, demonstrated that interfacial water configuration and the connectivity of H-bond networks in the EDL govern the HER activity[32]. Figure 2a exhibits the SEIRAS data acquired on different catalysts in Ar-saturated natural seawater at −0.05 V versus RHE. All the
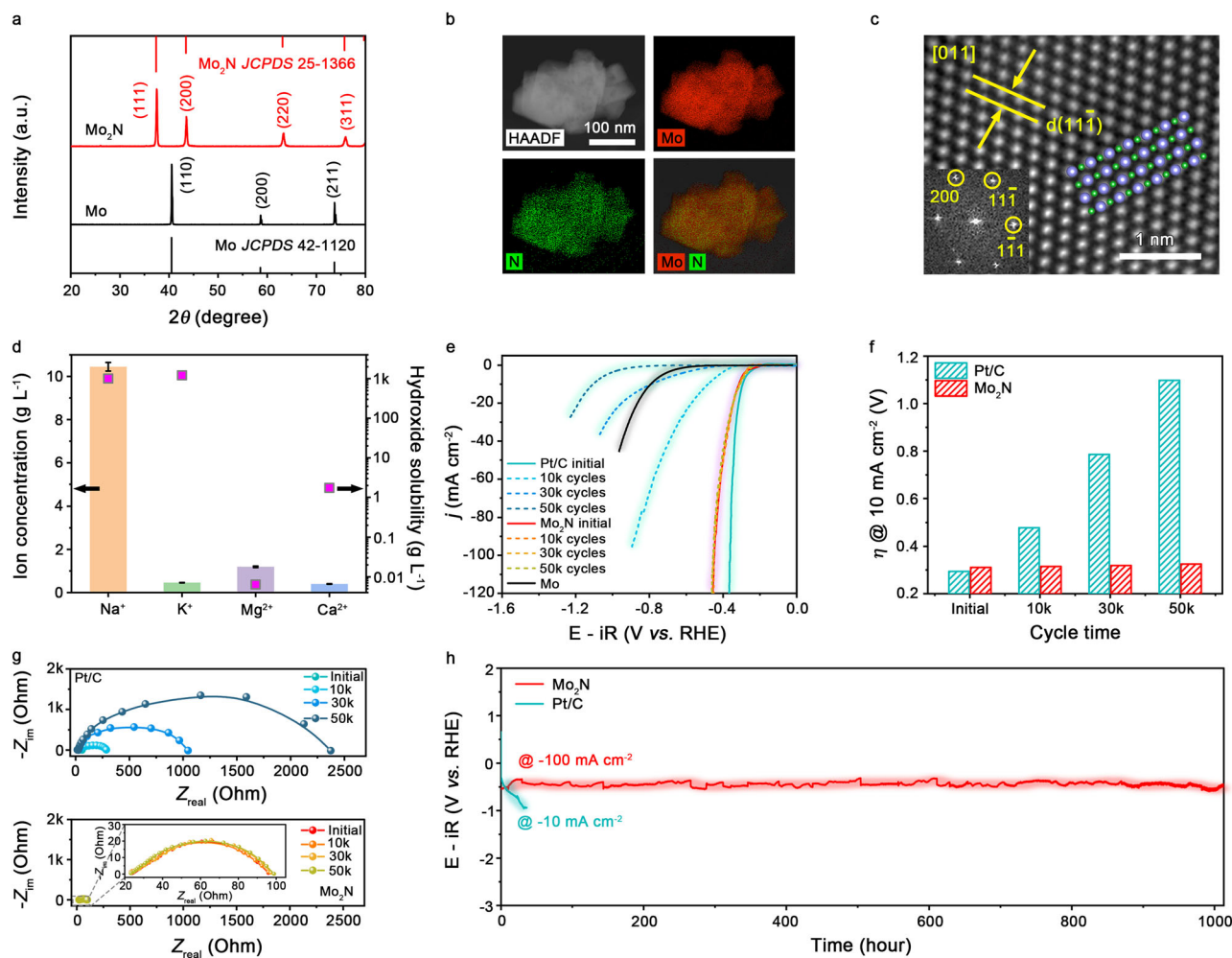
Fig. 1 | Electrocatalytic performance of Mo₂N in natural seawater. a XRD patterns of Mo and Mo₂N. **b** STEM-EDX elemental mapping of Mo₂N, showing the homogeneous distribution of Mo (red) and N (green), respectively. **c** HRTEM image of Mo₂N. Insets show the corresponding FFT pattern and atomic model viewed along the same direction. **d** The concentration of typical ions in natural seawater and the solubility of the corresponding hydroxides. Error bars are based on the standard deviation of three independent measurements. **e** HER polarization curves of Mo, Mo₂N, and commercial Pt/C catalysts before and after different potential cycles in natural seawater at room temperature (100% iR correction, where R was determined to be 23.7 ± 0.2 Ω). Catalyst loading: ~1.0 mg cm⁻². Sweep rate: 5 mV s⁻¹. Rotation rate: 1600 rpm. **f** The increase in overpotential at 10 mA cm⁻² for Mo₂N and Pt/C catalysts before and after different potential cycles. **g** EIS Nyquist plots of Mo₂N and Pt/C catalysts before and after different potential cycles. Inset shows the enlarged EIS Nyquist plots of Mo₂N. **h** Chronopotentiometry curves of Mo₂N and Pt/C catalysts performed in natural seawater.

samples showed a notable vibration band in the range of 1544.64–1724.83 cm⁻¹, which can be assigned to the H-O-H bending vibration band of interface water[32–34]. Gaussian fitting and deconvolution of the band revealed two distinct components corresponding to strongly H-bonded water (s-HB-H₂O at 1675.36 cm⁻¹) and weakly H-bonded water (w-HB-H₂O at 1632.42 cm⁻¹), respectively[33,34]. Noticeably, a band centered at ~1531.57 cm⁻¹ was observed for the TMN catalysts, attributed to the H-N-H bending vibration of NH₄⁺ (ref[35].), and its intensity increases following the order of Mo₂N > Ni₃N > TiN > ZrN > ScN₀.₉₈ > InN > YN (Fig. 2a). For metallic Mo, this band was absent. Therefore, we infer that surface lattice nitrogen would react with H adsorbed on TMNs during HER, forming NH₄⁺ species. The calculated N 2*p* projected density of states (PDOS) of the TMNs showed that their p-band centers vary with respect to the Fermi level (E_F) (Supplementary Fig. 19 and Supplementary Data 1). As the N 2*p* states move away from the E_F, the anti-bonding states below the E_F exhibit less nitrogen character, resulting in reduced covalency of metal-nitrogen bonds and, consequently, activated surface nitrogen[36,37]. Our PDOS calculations show a trend of Mo₂N > Ni₃N > TiN > ZrN > ScN₀.₉₈ > InN > YN. This trend correlated with the trend of the spectroscopic

measurement of NH₄⁺ signals of the seven TMNs, among which Mo₂N yielded the most NH₄⁺ species owing to its lowest covalency between Mo and N (Fig. 2b).

The normalized integrated NH₄⁺ peak area relative to that of interfacial H₂O was plotted as a function of the proportion of s-HB-H₂O for each TMN catalyst. Figure 2c reveals a positive correlation between NH₄⁺ and s-HB-H₂O, implying that NH₄⁺ benefits the formation of interfacial water with strong H-bond interactions (Supplementary Fig. 20). The direct evidence for the existence of NH₄⁺ is provided by operando differential electrochemical mass spectroscopy (DEMS) measurements in natural seawater (Supplementary Fig. 21). Holding the electrode at −10 mA cm⁻² yielded a considerable mass-to-charge signal (m/z) for H₂ (m/z = 2), which attenuated rapidly once the applied current was removed (Fig. 2d). Immediately afterwards, a sharp signal of NH₃ (m/z = 17) appeared. Under negative electric field, the in situ formed NH₄⁺ species were attracted in the EDL, which accumulated and were released to generate NH₃ when the electrode surface turned electrically neutral. The formation of NH₄⁺ can be further confirmed by the ¹H nuclear magnetic resonance (¹H NMR) spectra and ion chromatography (Supplementary Fig. 22 and Supplementary Table 6).
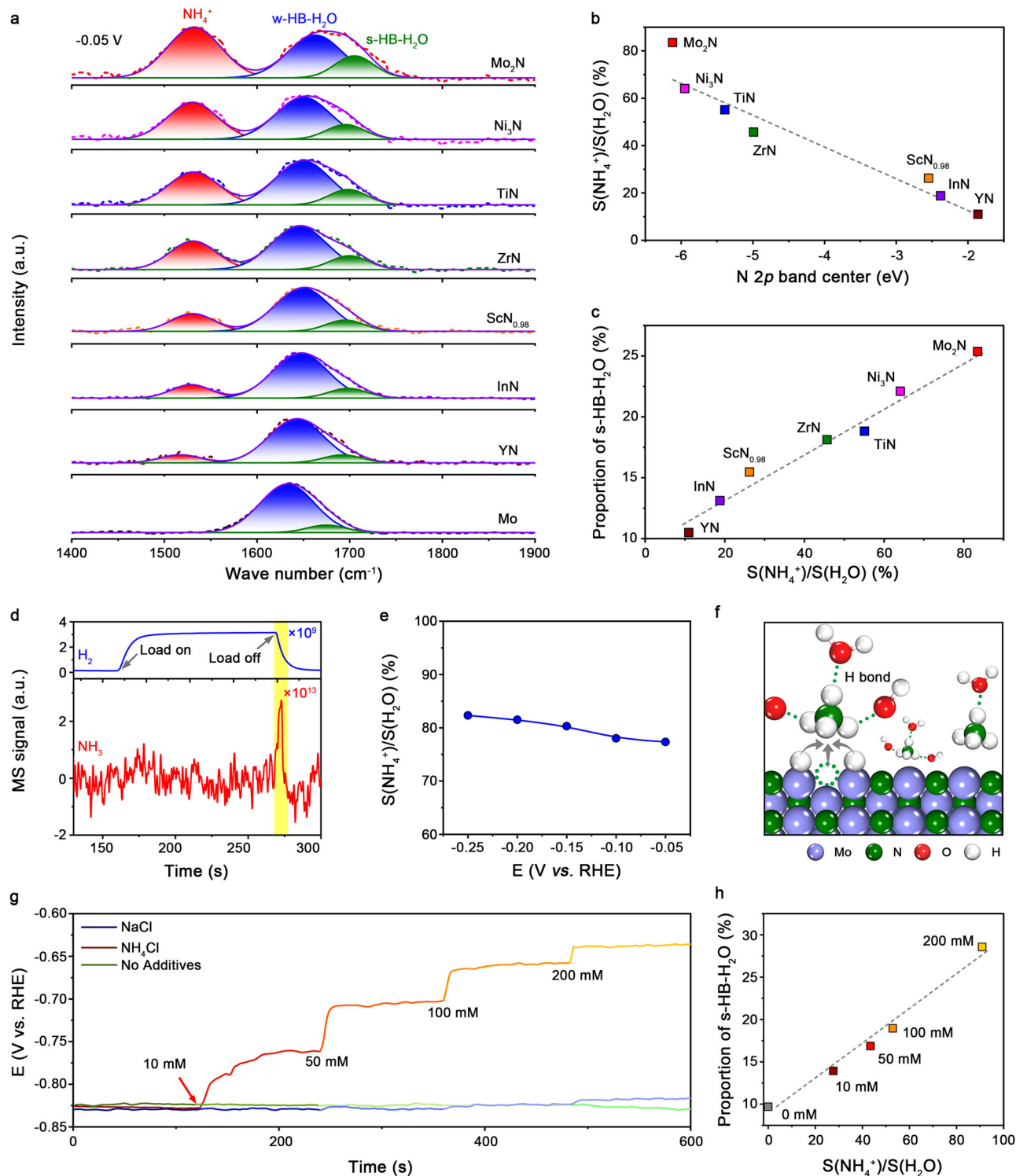
Fig. 2 | In situ NH_4^+ formation at the catalyst surface. a In situ SEIRAS spectra of different metal nitrides at −0.05 V in Ar-saturated natural seawater. **b** The proportion of NH_4^+ species in the EDL versus N $2p$ band center for different metal nitrides. **c** The proportion of s-HB-H_2O versus the proportion of NH_4^+ species in the EDL for different metal nitrides. **d** Online electrochemical DEMS measurements over Mo_2N catalyst in natural seawater. **e** The proportion of NH_4^+ species in the EDL of the Mo_2N catalysts as a function of applied potentials. The proportion of NH_4^+ in the EDL were extracted from the in situ SEIRAS spectra in Supplementary Fig. 23.

f Schematic of the NH_4^+ formation on the Mo_2N surface. **g** Chronopotentiometry curves of Mo operated at −10 mA cm^{-2} in natural seawater with different concentration of NH_4Cl and NaCl, respectively. The pH of the bulk seawater was fixed at 7.84 by adding NaOH. **h** The proportion of s-HB-H_2O versus the proportion of NH_4^+ species in the EDL for the Mo catalyst operated at −0.05 V in Ar-saturated natural seawater with different concentrations of NH_4Cl. The proportion of s-HB-H_2O and the proportion of NH_4^+ were extracted from the in situ SEIRAS spectra in Supplementary Fig. 24.

Additionally, the NH_4^+ population on Mo_2N surface increases linearly with increasing the applied negative bias (Fig. 2e and Supplementary Fig. 23).

In natural seawater, the high concentration of alkaline cations (Fig. 1d) makes them easily be migrated to catalyst surface at negative bias owing to the electrostatic effect. The enriched cations in the EDL would cause the loss of their partial solvation, promoting w-HB-H_2O molecules and thus raising the barrier of hydrogen transfer at electrochemical interface[33,38,39]. Over Mo_2N catalyst, NH_4^+ groups are generated in situ at the surface at negative potential and can interact with H_2O and hydroxyl in the EDL[35,40,41], giving rise to increased connectivity of H-bond networks and, consequently, more s-HB-H_2O molecules (Fig. 2f). We also performed operando electrochemical impedance spectroscopy (EIS) at different overpotentials in Ar-saturated seawater to probe hydrogen adsorption resistance and hydrogen adsorption pseudo-capacitance for Mo and Mo_2N catalysts[42,43] (Supplementary Fig. 25). Our experimental results indicate that Mo_2N has greatly lower hydrogen adsorption resistance and higher adsorbed hydrogen than that for Mo at all biases examined, indicating that NH_4^+ species in the Stern layer improve H-bond networks for better hydrogen transfer and adsorption. To validate the enhancement of HER by NH_4^+ species, we carried out galvanostatic measurements of metallic Mo at 10 mA cm^{-2} with the addition of NH_4Cl. Figure 2g shows that the overpotential decreased from about 761.8 to 637.4 mV with increasing the NH_4^+ amount from 10 to 200 mM. Accordingly, in situ SEIRAS analyses showed that the s-HB-H_2O populations at −0.05 V increased from 13.9% to 28.6% (Fig. 2h and Supplementary Fig. 24). Without NH_4^+ addition, no reduced overpotential was observed. Moreover, the addition of NaCl instead of NH_4Cl also cannot bring overpotential reduction. The critical role of NH_4^+ in making s-HB-H_2O, which shows positive correlation with the connectivity of H-bond networks, and thus enhancing HER energetics was also evidenced by the linear sweep voltammetry measurements with and without NH_4Cl addition (Supplementary Fig. 26).

Origin of anti-precipitation capability

To track the evolution of the surface product and corresponding phase not observable by RDE measurements, the Mo_2N and Pt/C dispersions were sprayed uniformly onto carbon papers at a loading of 1 mg cm^{-2}, which we then used for galvanostatic experiments by holding the electrodes at different current densities. The Pt/C electrode showed slow degradation at −1 and −3 mA cm^{-2}, and enormous degradation at −10 mA cm^{-2} (Fig. 3a). The initial and spend electrodes were visualized by a series of photographs, showing that the electrodes were gradually covered with white precipitates as the applied current increases (Fig. 3b). XRD patterns exhibited a majority $Mg(OH)_2$ phase, and no diffraction peaks from $Ca(OH)_2$ could be observed (Fig. 3c). This is not unexpected, as the high seawater Mg^{2+} concentration and the low solubility of $Mg(OH)_2$ (Fig. 1d). These results are in marked contrast to Mo_2N electrode on which $Mg(OH)_2$ formation was completely prohibited even up to −100 mA cm^{-2} (Fig. 3d–f). We note that, as the current density increases, the diffraction corresponding to Mo_2N (111) facets shifted gradually to higher angles (Supplementary Fig. 27), which indicates the formation of nitrogen vacancies[44], consistent with our electron paramagnetic resonance (EPR) measurements[45] (Supplementary Fig. 28). Additionally, only surface lattice nitrogen on Mo_2N can migrate out to form NH_4^+, while lattice nitrogen from inner Mo_2N is inactive (Supplementary Figs. 29 and 30). In general, $Mg(OH)_2$ would form when solution pH is greater than 9.5 (ref.[12].). We speculate that the in situ formed NH_4^+ groups play an important role in confining the locally generated OH^- groups during HER through hydrogen-bond interaction. To support this view, an IrO_x-modified rotating RDE (RRED) measurement was employed to quantitatively probe pH on Mo_2N and Pt/C electrode surfaces in natural seawater[46]

(Supplementary Figs. 31, 32). As Fig. 3g shows, the pH value on Pt/C surface exhibited a sharp increase (from 8.26 to 11.65) with increasing the applied current density from −0.3 to −10 mA cm^{-2}. The surface pH on Mo_2N also increased, but in a much slower manner, which reached mere 9.05 at even −100 mA cm^{-2}, thus avoiding $Mg(OH)_2$ formation. Density functional theory (DFT) simulations predict that hydrogen of the NH_4^+ is poised to form strong hydrogen-bond interactions with H_2O and OH^- groups (Supplementary Fig. 33 and Supplementary Data 1), consistent with previous reports[40,41]. As a result, OH^- generated from the water dissociation during HER was constrained by NH_4^+ in the Stern layer, suppressing the pH increase.

From our analysis, the electrocatalytic HER performance of Mo_2N in natural seawater can be understood from the proposed mechanism shown in Fig. 3h. Under negative bias, surface nitrogen on Mo_2N was activated and reacted with the adsorbed H that generated during the HER process, forming NH_4^+ species. These NH_4^+ groups were confined in the EDL via electrostatic interaction and strongly H-bonded to hydroxyl and interfacial water, which improved the connectivity of H-bond networks, facilitating high-efficiency proton transfer in the interfacial region. On one hand, this more connected H-bond network with reduced hydrogen transfer barrier can greatly enhance the HER kinetics. What's more, the H-bonded OH^- groups were confined in the Stern layer and can barely diffuse out of the EDL, thus suppressing the rise of pH and, consequently, the formation of hydroxide precipitates. We notice that the attack from Cl^- toward the Mo_2N cathode is negligible owing to the weak binding strength between Cl and Mo_2N surface (Supplementary Figs. 34 and 35 and Supplementary Data 1).

Performance in a practical electrolyser

To further corroborate the outstanding performance described above, we incorporated Mo_2N catalyst (1.0 mg cm^{-2}) in the cathode of a 25-cm^2 membrane electrode assembly (Fig. 4a) and tested it in a practical water electrolyser at 60 °C (see Methods, Supplementary Fig. 36). At the anode, commercial IrO_2 was used as catalyst with a loading of 1.0 mg$_{Ir}$ cm^{-2}. Considering that IrO_2 can suffer from chloride attack in natural seawater electrolysis[47], simulated seawater with 1.19 g L^{-1} $MgSO_4$ and 0.40 g L^{-1} $CaSO_4$ was used as the feed. Figure 4b shows the current-voltage polarization curve of Mo_2N catalyst in the electrolyser, which required a voltage of 1.87 V to reach the industrially relevant current density of 1 A cm^{-2}. By comparison, the electrolyser with Pt/C cathode displayed a cell voltage of 1.68 V at 1 A cm^{-2}, showing only 190 mV advantage over the nonprecious Mo_2N catalyst. When operating at 1 A cm^{-2}, the energy efficiency of our electrolyser with Mo_2N cathode arrived at 65.9%, corresponding to an energy consumption of 50.0 kWh kg^{-1} H_2 (see Supplementary materials for calculation details).

We also performed long-term stability measurement of the electrolyser with Mo_2N cathode at the current density of 1 A cm^{-2} and 60 °C. Figure 4c shows that the device run steadily over 900 hours with no appreciable voltage increase. The performance metrics of Mo_2N are superior when compared with previous non-noble cathodes tested in pure water and seawater (Supplementary Table 7). By contrast, Pt/C cathode underwent a notable decay with a degradation rate of 2.16 mV h^{-1}, originating from the formation of $Mg(OH)_2$ precipitate (Supplementary Fig. 37). During electrolysis, the cations, such as Na$^+$, will replace with H$^+$ and cause the lack of H$^+$ at cathode. Consequently, the reduction of H_2O happens at cathode, leading to a steep pH increase[48]. Furthermore, we determined experimentally the H_2 production rate of about 10.45 L h^{-1} from the Mo_2N-drove electrolyser at 1 A cm^{-2} (Fig. 4d), corresponding to a H_2 cost of US$1 per kilogram (see Methods for calculation details), half that of the US Department of Energy target of US$2 per kilogram[49]. No NH_3 impurity can be detected by the gas chromatography−mass spectrometry in the as-produced H_2 (Supplementary Fig. 38).
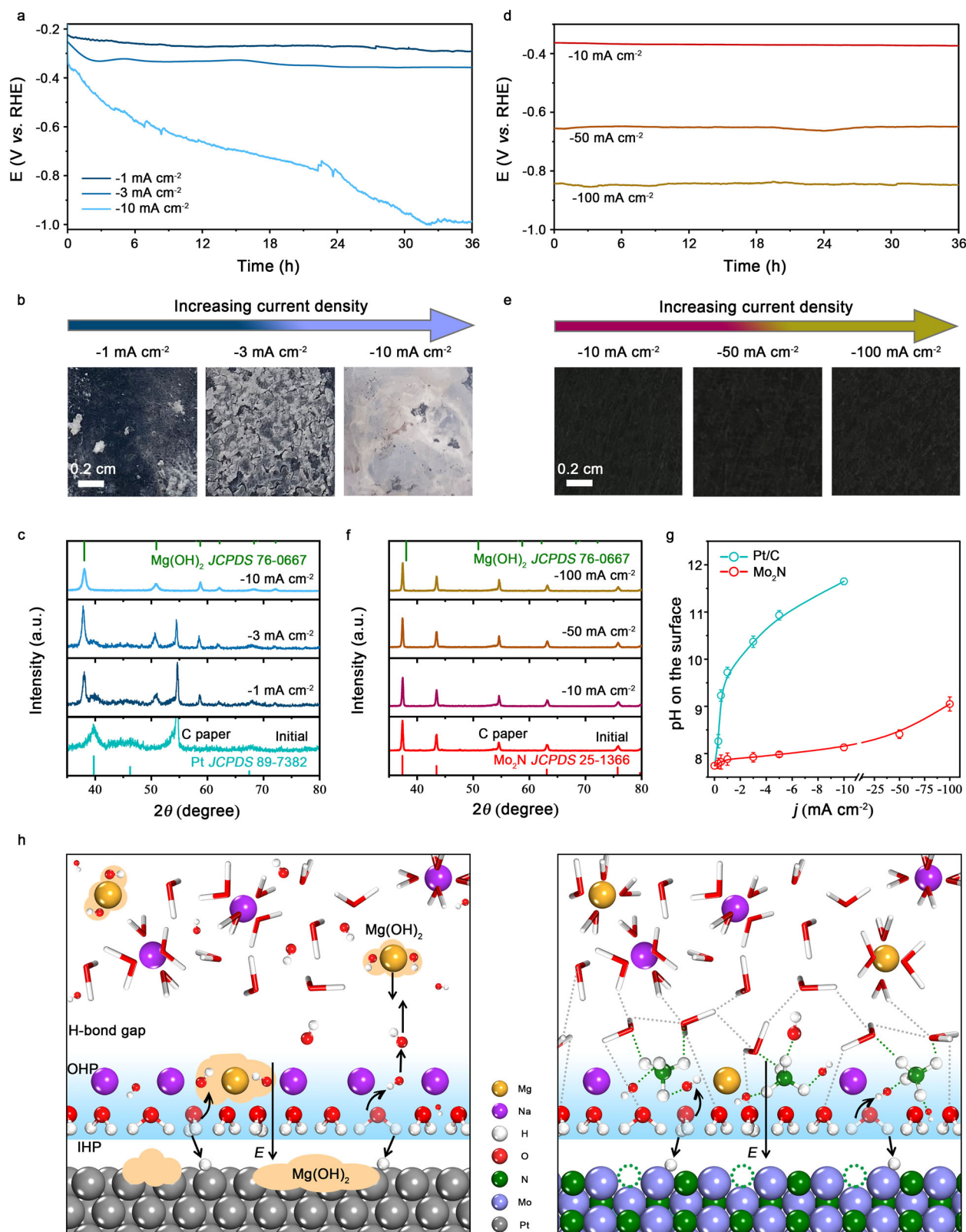
Fig. 3 | Anti-precipitation capability of Mo$_2$N catalyst. a, d Chronopotentiometry curves of commercial Pt/C (**a**) and Mo$_2$N (**d**) catalysts operated at different current density in natural seawater. **b, e** Photographs of Pt/C (**b**) and Mo$_2$N (**e**) catalysts on the carbon paper after electrolysis at different current densities for 36 hours in natural seawater. **c, f** XRD patterns of Pt/C (**c**) and Mo$_2$N (**f**) catalysts on the carbon paper after electrolysis at different current densities for 36 hours in natural seawater. **g** Local pH on the surface of Pt/C and Mo$_2$N catalysts as a function of current density in natural seawater. Error bars are based on the standard deviation of three independent measurements. **h** Schematic of the NH$_4^+$ formation on the Mo$_2$N surface that prevents precipitate formation, whereas Mg(OH)$_2$ precipitate formed on the surface of Pt/C catalyst.
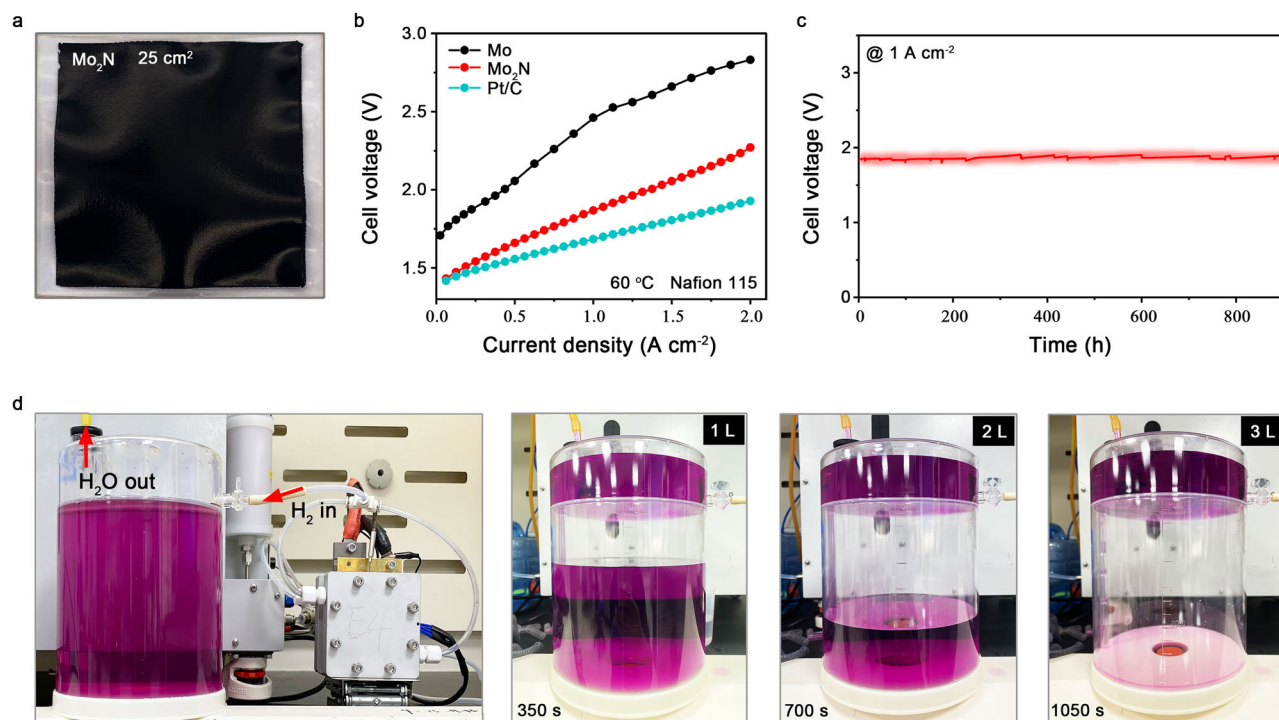
Fig. 4 | Electrolyser performance. a Photograph of Mo_2N catalyst on Nafion 115 membrane. Catalyst loading: $1.0\ mg\ cm^{-2}$. **b** Current-voltage polarizations of the zero-gap membrane flow electrolyser using Mo, Mo_2N, and commercial Pt/C as the cathodic catalysts. **c**, Chronopotentiometry measurement of the electrolyser at $1\ A\ cm^{-2}$ and 60 °C for Mo_2N cathodic catalyst. **d**, Photograph of the zero-gap membrane flow electrolyser with Mo_2N cathode, showing that 3 L H_2 was obtained after 1050 s at $1\ A\ cm^{-2}$ and 60 °C.

Discussion

In conclusion, high-quality Mo_2N catalyst with enhanced HER activity and stability in seawater electrolysis was synthesized through a convenient and scalable plasma-enhanced CVD route. The catalyst can generate NH_4^+ groups in situ on its surface, which limits local pH increase in the vicinity of the electrode, thus preventing the formation of hydroxide precipitates during seawater electrolysis. Meanwhile, these NH_4^+ species also greatly improve the connectivity of the H-bond networks in the EDL region, leading to the enhanced HER energetics. We have showed of how ammonium groups formed at the catalyst surface can improve catalytic activity and simultaneously avoid hydroxide formation. We foresee that these findings will stimulate further tuning of catalyst microenvironments for highly efficient seawater splitting.

Methods

Material synthesis

Scandium powder (Sc, 99.9 %), titanium powder (Ti, 99.99 %), nickel powder (Ni, 99.99 %), yttrium powder (Y, 99.9 %), zirconium powder (Zr, 99.5 %), molybdenum powder (Mo, 99.5 %) and indium powder (In, 99.99 %) were purchased from Innochem. The dinitrogen (N_2, 99.999%) was purchased from Nanjing Special Gas Factory Co., Ltd, China. All the chemicals were used as received without further purification.

The metal nitrides were prepared by the plasma-enhanced chemical vapor deposition. Briefly, the metal powder was subjected to the N_2 plasma treatment in the chamber of the radio frequency-plasma enhanced chemical vapor deposition (RF-PECVD) systems under a pressure of 0.02 Torr. After the temperature of the chamber reached the synthetic temperature, the radio frequency-plasma discharge was conducted at 300 W and 13.56 MHz for 30 min. The synthetic temperature used for each nitride, as well as their structural information were summarized in Supplementary Table 1.

Material characterization

The study employed Transmission Electron Microscopy (TEM) analysis, High-Resolution Transmission Electron Microscopy (HRTEM) measurements, and Energy Dispersive Spectroscopy (EDS) mappings using a FEI Talos F200X. This instrument is equipped with a Super X-EDS system, which comprises four systematically arranged windowless silicon drift detectors, operating at 200 kV. High-resolution HAADF images were obtained using the JEM-ARM 200 F Atomic Resolution Analytical Microscope, which operates with an acceleration voltage of 200 kV. Scanning electron microscope (SEM) images were captured utilizing the Zeiss Supra 40 apparatus.

X-ray powder diffraction (XRD) data were acquired using a Japan Rigaku DMax-γA rotation anode X-ray diffractometer, calibrated with graphite monochromatized Cu-K radiation. The Raman spectra was conducted using a LABRAM-HR confocal laser micro-Raman spectrometer, equipped with a 532 nm wavelength. X-ray photoelectron spectroscopy (XPS) data were collected using an ESCALAB-MKII x-ray photoelectron spectrometer, with Mg Kα radiation serving as the excitation source (Mg Ka = 1253.6 eV). The XAFS spectra were gathered at the 1W1B station of the Beijing Synchrotron Radiation Facility. The ion chromatography data were derived from the ICS-3000 instrument.

Density functional theory calculation

The Vienna Ab-initio Simulation Package (VASP) software[50], a plane-wave code, was utilized to carry out all the spin-polarized density functional theory (DFT) calculations. These calculations were conducted within the Generalized Gradient Approximation (GGA) framework, employing the Perdew-Burke-Ernzerhof (PBE) formulation[51]. The projected augmented wave (PAW) potentials[52] were selected to characterize the ionic cores and incorporate valence electrons. This was achieved using a plane wave basis set, with a kinetic energy cutoff of 500 eV. Partial occupancies of the Kohn-Sham orbitals were permitted using the Gaussian smearing technique, with a width of 0.02 eV. Electronic energy was deemed self-consistent when the energy change fell

below 10^{-6} eV. Hubbard U corrections were implemented for the transition metal d-electrons. The U–J parameters for Sc (3.28), Ti (5.61), Ni (3.80), Cu (3.08), Y (1.98), Zr (2.61), and Mo (3.28) atoms were subsequently adopted.

Electrochemical measurement

All electrochemical measurements were conducted utilizing a standard three-electrode cell at ambient temperature, interfaced with a VSP-300 potentiostat (BioLogic, France). The Ag/AgCl electrode, saturated in 3.5 M KCl, served as the reference electrode, while the graphite rod functioned as the counter electrode. The potential documented in this study were normalized relative to the RHE, employing a standard RHE calibration equation: $E_{RHE} = E_{Ag/AgCl} + (0.196 + 0.059\, pH)$ V. The working electrode, a rotating disk electrode (RDE), was fabricated using glassy carbon (PINE, with a diameter of 5.00 mm and a disk area of 0.196 cm^2). The RDE was meticulously polished using α-Al$_2$O$_3$ powder of progressively decreasing sizes (ranging from 1.0 to 50 nm). Subsequently, it was ultrasonically cleansed with deionized water and absolute ethanol. The catalyst powder, weighing 5 mg, was dispersed in 1 ml of a 1:3 v/v isopropanol/deionized water (DIW) solution, containing 40 μL of a 5 wt% Nafion solution. This mixture was ultrasonicated to generate a homogeneous ink.

For the electrochemical measurements of the hydrogen evolution reaction (HER), a volume of 40 μl of catalyst ink was deposited on a glassy carbon electrode, yielding a catalyst loading of approximately 1.0 mg cm^{-2}. Prior to conducting the HER measurements, 200 mL of freshly electrolytes (seawater with a pH of 7.84 ± 0.02, sourced from the Gulf of Mexico, specifically the Gulf Stream off Dauphin Island, Alabama, and supplied by Sigma-Aldrich under the product code S9148) were purged with pure argon for a duration of 30 minutes. The polarization curves of HER were documented at a rate of 5 mV s^{-1} and 1600 r.p.m (to eliminate the formation of H$_2$ bubbles in situ) under ambient conditions. The accelerated stability measurements were conducted through potential cycling between −0.2 V and −0.4 V relative to RHE, with a sweep rate of 200 mV s^{-1}. Subsequently, the electrode underwent polarization curves with a sweep rate of 5 mV s^{-1}.

The electrochemical impedance spectroscopy (EIS) measurement was executed under a constant overpotential of 300 mV, spanning a frequency range from 100 kHz to 100 mHz. The sinusoidal voltage amplitude was set at 5 mV. The polarization curves were re-configured to represent overpotential (η) against the logarithm of current (log j) to generate Tafel plots for the evaluation of the HER kinetics of the examined catalysts. The Tafel slope (b) was derived by fitting the linear section of the Tafel plots to the Tafel equation (η=blog(j)+a). The exchange current density (j$_0$) was subsequently calculated from the Tafel curves employing an extrapolation technique.

The working electrode, comprised of Mo$_2$N-modified carbon paper with a catalyst loading of approximately 1.0 mg cm^{-2}, was utilized to perform chronopotentiometry experiments at a constant current density of 100 mA cm^{-2}. To gauge the double-layer capacitance, cyclic voltammograms were taken at various sweep rates within the potential range of −0.05 to 0.05 V relative to RHE, under ambient temperature conditions. All polarization curves were adjusted with iR compensation, derived from the resistance of the solution.

The process of CO stripping was initiated by maintaining the electrode potential at 0.1 V relative to RHE for a duration of 10 minutes, allowing for the adsorption of CO on the catalyst surface. Subsequently, an Ar purge was conducted for 30 minutes to eliminate any residual CO present in the electrolyte. The CO stripping current was then determined using cyclic voltammetry within a potential range of 0 to 1.2 V, with a sweep rate of 20 mV s^{-1}.

The ECSA of the catalyst is determined using the double-layer capacitance, calculated from the equation:

$$ECSA = \frac{C_{dl}}{C_s} \tag{1}$$

The specific capacitance, denoted as C$_s$, refers to the capacitance of a catalyst or an atomically smooth, planar surface of a material, per unit area, under identical electrolyte conditions. A general value of C$_s$ = 0.030 mF cm^{-2} is commonly adopted, based on the typical reported data[53].

NMR measurement

In the context of ^{1}H nuclear magnetic resonance (^{1}H NMR) measurement, a carbon fiber paper modified with Mo$_2$N served as the working electrode (catalyst loading: ~1.00 mg cm^{-2}; area: 10 cm^2) and 15 mL Ar-saturated natural seawater was used as the electrolyte. Subsequently, HER was conducted at −10 mA cm^{-2} for a duration of 10 minutes, and the above operation was repeated twenty times with a newly prepared Mo$_2$N-modified carbon fiber paper before collecting the electrolyte. The pH of the post-reaction electrolyte was subsequently adjusted to 2 through the addition of HCl. Then, 500 μL of electrolyte was combined with 100 μL of D$_2$O, which contained 50 ppm (m/m) of dimethyl sulfoxide (DMSO) as the internal standard. Uniform spectral acquisition parameters were employed across all measurements to guarantee thorough relaxation and accurate quantification. The ^{1}H NMR signal, with water suppression mode, was recorded utilizing a Bruker 400 MHz system.

Zero-gap membrane flow electrolyser measurement

The preparation of the catalyst ink involves dispersing the catalyst and a 5 wt% Nafion solution in ethanol. This mixture is subsequently subjected to ultrasonication to achieve a homogeneous ink. For the creation of the catalyst-coated membrane (CCM), the anode (IrO$_2$) and cathode (Mo$_2$N) catalysts are sprayed onto sheets of polytetrafluoroethylene (PTFE)-coated glass fiber fabric, respectively. Subsequently, the cathode catalysts, supported on PTFE-coated glass fiber fabric and Nafion 115, and the anode catalysts, supported on PTFE-coated glass fiber fabric, are subjected to hot pressing. This process is conducted at a temperature of 150 °C for a duration of 5 minutes, applying a pressure of 10 tons. Following the cooling process, the PTFE-coated glass fiber fabric was meticulously removed to achieve the CCM with an electrode area of 25 cm^2. The final catalyst loadings were set at 1.0 mg$_{Ir}$ cm^{-2} for the anode and 1.0 mg Mo$_2$N cm^{-2} for the cathode. The prepared CCM was subsequently stored in distilled water for further measurements.

To evaluate the performance of the zero-gap membrane flow electrolyser, a titanium felt coated with platinum was utilized as the porous transport layer (PTL) at the anode. In contrast, a titanium felt without platinum coating served as the PTL at the cathode. The zero-gap membrane flow electrolyser was operated at a temperature of 60 °C. Simulated seawater, composed of 1.19 g L^{-1} MgSO$_4$ and 0.40 g L^{-1} CaSO$_4$, served as the reactant for the constructed zero-gap membrane flow electrolyser. The electrolyser was supplied via a peristaltic pump circulation system.

Hydrogen production rate

The drainage technique is employed to accumulate hydrogen over a specified timeframe in order to ascertain the rate of hydrogen production. Briefly, fill the cylinder with water and position it in the sink with its mouth submerged below the water level. Subsequently, place the gas outlet beneath the bottle's mouth. As the water drains from the bottle, it is simultaneously replaced by gas. The rate of H$_2$ production is ~10.45 L h^{-1} when the zero-gap membrane flow electrolyser operates at a current density of 1 A cm^{-2} and a temperature of 60 °C.

Energy efficiency calculation

The calculation of energy efficiency for a zero-gap membrane flow electrolyser is predicated on the subsequent equation:

$$\text{Energy efficiency} = \frac{1.23V}{U_{cell}} \times FE \qquad (2)$$

The value of 1.23 V represents the theoretical energy of the products, while U_{cell} denotes the cell voltage (V) necessary to deliver a current density of 1 A cm^{-2}. The Faradaic efficiency (FE) for the conversion of H_2O to H_2, quantified here, is 99.95%.

Energy consumption calculation

The energy consumption of the zero-gap membrane flow electrolyzer is determined using the subsequent equation:

$$\text{Energy consumption} = \frac{U_{cell}I_{cell}t}{m} \qquad (3)$$

I_{cell} refers to the current delivered (A), t represents the operational time (h), and m denotes the mass of hydrogen produced over a period of t.

Hydrogen production cost calculation

The electricity cost is calculated based on the energy consumption demonstrated above:

$$\text{Cost}(H_2/kg) = \text{energy consumption} \times \text{electricity bill} \qquad (4)$$

where energy consumption is calculated at 1 A cm^{-2}, with the electricity bill being \$0.02/Kw h.

Local pH on the catalyst surface

In this study, we utilized a rotating ring-disk electrode (RRDE), modified with IrO_x, to measure the local pH on the catalyst surfaces. First, we prepared the electrodeposition solution of IrO_x in accordance with Yamanaka's method[46]. Subsequently, we electrodeposited the IrO_x film onto the Pt ring electrode of the RRDE using cyclic voltammetry. Next, the pH dependence of the open circuit potential (E_{ocp}) in seawater was quantified utilizing an IrO_x ring electrode. The correlation between E_{ocp} and the pH value of the ring electrode (pH_{ring}) is established through the subsequent equation:

$$pH_{ring} = a \times (E_{ocp} + b) \qquad (5)$$

The values of a and b were derived from the linear regression analysis conducted on the relationship between E_{ocp} and the pH values of the bulk seawater (Supplementary Fig. 32). Subsequently, we conducted a measurement of local pH on the catalyst surface, varying the current density. We applied different constant current densities to the catalyst-coated disk electrode immersed in seawater. Simultaneously, we recorded the E_{ocp} using an IrO_x ring electrode. The pH value of the IrO_x ring electrode was determined using the E_{ocp} and Eq. (5). To ascertain the pH value of the catalyst-coated disk electrode, the pH value of the IrO_x ring electrode was utilized in the subsequent equation:

$$C_{H^+,ring} - C_{OH^-,ring} = N_D \times (C_{H^+,ring} - C_{OH^-,ring}) \\ + (1 - N_D) \times (C_{H^+,bulk} - C_{OH^-,bulk}) \qquad (6)$$

The concentrations of H^+ ions on the ring electrode, disk electrode, and the bulk seawater are denoted as $C_{H^+,ring}$, $C_{H^+,disk}$ and $C_{H^+,bulk}$, respectively. And the concentrations of OH^- on the ring electrode, disk electrode and the bulk seawater are denoted as $C_{OH^-,ring}$, $C_{OH^-,disk}$ and $C_{OH^-,bulk}$, respectively. In addition, the value of $N_D = 0.275$ represents the collection efficiency.

In situ SEIRAS experiment

Firstly, it is necessary to prepare the gold film for SEIRAS. The process begins with washing the silicon prism using an aqua regia solution. Subsequently, the prism is polished with a 0.05 μm Al_2O_3 slurry, and then it undergoes ultrasound treatment in acetone and deionized water, respectively. Following this, the prism is dried and immersed in a NH_4F solution for 120 seconds. The final step involves submerging the silicon prism in a mixture of a gold-plated solution and a 2 wt % HF aqueous solution at a temperature of 55 °C for 7 minutes, thereby chemically depositing the gold film. Following deposition, the gold film on the silicon prism was rinsed with deionized water (DIW). Subsequently, the working electrodes were prepared by applying ink onto the gold film. A catalyst powder of 10 mg was dispersed in 1 mL of isopropanol. The mixture was subjected to ultrasonication to create a homogeneous ink. Then, 200 μL of the catalyst ink was evenly pipetted onto the gold film. Lastly, the working electrode was allowed to dry naturally.

In situ SEIRAS tests were conducted using a spectroelectrochemical cell with a three-electrode configuration. A graphite rod served as the counter electrode, while a saturated Ag/AgCl acted as the reference electrode. The cell was incorporated into a NICOLET iS50 FTIR spectrometer, which featured a liquid nitrogen-cooled MCT detector. Throughout the in situ SEIRAS test, a continuous flow of Ar was maintained within the electrolyte. Furthermore, each spectrum was composed of 32 individual beams, each with a resolution of 4 cm^{-1}.

In situ DEMS measurements

In situ DEMS measurements were carried on a Linglu QMG 250 device, which was fitted with a high vacuum chamber linked to a molecular pump. An electrochemical cell was linked to this vacuum chamber through a cold trap, which was cooled using dry ice. This configuration was specifically designed to capture water vapor for introduction into the mass spectrometer. For the process of gas-liquid separation, the working electrode was constructed by depositing gold onto a 50 μm thick, porous polytetrafluoroethylene (PTFE) membrane. Characterized by a pore size of 0.2 μm and a porosity of 85%, this membrane served as the foundation for the electrode. Subsequently, catalyst ink was applied to a gold-coated membrane, with a loading of roughly 1.0 mg cm^{-2}. A saturated Ag/AgCl electrode functioned as the reference electrode, while a graphite rod served as the counter electrode. The experiments were conducted in seawater, with the electrolyte saturated by Ar bubbling prior to electrochemical measurements. A mass spectrometer monitored the gaseous products, of varying molecular weights, generated during the HER in real-time.

Data availability

Source data are provided with this paper.

References

1. Turner, J. A. Sustainable hydrogen production. *Science* **305**, 972–974 (2004).
2. Rashid, M., Al Mesfer, M. K., Naseem, H. & Danish, M. Hydrogen production by water electrolysis: a review of alkaline water electrolysis, PEM water electrolysis and high temperature water electrolysis. *Int. J. Eng. Adv. Technol.* **4**, 80–93 (2015).
3. Chatenet, M. et al. Water electrolysis: from textbook knowledge to the latest scientific strategies and industrial developments. *Chem. Soc. Rev.* **51**, 4583–4762 (2022).

4. Dresp, S., Dionigi, F., Klingenhof, M. & Strasser, P. Direct electrolytic splitting of seawater: opportunities and challenges. *ACS Energy Lett.* **4**, 933–942 (2019).

5. Khan, M. A. et al. Seawater electrolysis for hydrogen production: a solution looking for a problem? *Energ Environ Sci* **14**, 4831–4839 (2021).

6. Tong, W. et al. Electrolysis of low-grade and saline surface water. *Nat. Energy* **5**, 367–377 (2020).

7. Jin, H. et al. Emerging materials and technologies for electro-catalytic seawater splitting. *Sci. Adv.* **9**, eadi7755 (2023).

8. Wang, N. et al. Strong-proton-adsorption co-based electrocatalysts achieve active and stable neutral seawater splitting. *Adv. Mater.* **35**, e2210057 (2023).

9. Xu, W. et al. Ag nanoparticle-induced surface chloride immobili-zation strategy enables stable seawater electrolysis. *Adv. Mater.* **35**, e202306062 (2023).

10. Kang, X. et al. A corrosion-resistant RuMoNi catalyst for efficient and long-lasting seawater oxidation and anion exchange membrane electrolyzer. *Nat. Commun.* **14**, 3607 (2023).

11. Yu, H., Wan, J., Goodsite, M. & Jin, H. Advancing direct seawater electrocatalysis for green and affordable hydrogen. *One Earth* **6**, 267–277 (2023).

12. KAPP, E. M. The precipitation of calcium and magnesium from sea water by sodium hydroxide. *Biol. Bull.* **55**, 453–458 (1928).

13. Farràs, P., Strasser, P. & Cowan, A. J. Water electrolysis: direct from the sea or not to be? *Joule* **5**, 1921–1923 (2021).

14. Ros, C. et al. Facing seawater splitting challenges by regeneration with Ni–Mo–Fe bifunctional electrocatalyst for hydrogen and oxy-gen evolution. *ChemSusChem* **14**, 2872–2881 (2021).

15. Li, P. et al. Common-ion effect triggered highly sustained seawater electrolysis with additional NaCl production. *Research* **2020**, 2872141 (2020).

16. Xie, H. et al. A membrane-based seawater electrolyser for hydrogen generation. *Nature* **612**, 673–678 (2022).

17. Wu, L. et al. Heterogeneous bimetallic phosphide Ni_2P-Fe_2P as an efficient bifunctional catalyst for water/seawater splitting. *Adv. Funct. Mater.* **31**, 2006484 (2021).

18. Liu, H. et al. High-performance alkaline seawater electrolysis with anomalous chloride promoted oxygen evolution reaction. *Angew. Chem. Int. Ed.* **62**, e202311674 (2023).

19. Kuang, Y. et al. Solar-driven, highly sustained splitting of seawater into hydrogen and oxygen fuels. *Proc. Natl. Acad. Sci. USA.* **116**, 6624–6629 (2019).

20. Chong, L. et al. La- and Mn-doped cobalt spinel oxygen evolution catalyst for proton exchange membrane electrolysis. *Science* **380**, 609–616 (2023).

21. Stiber, S. et al. A high-performance, durable and low-cost proton exchange membrane electrolyser with stainless steel components. *Energy Environ. Sci.* **15**, 109–122 (2022).

22. Shi, Z. et al. Enhanced acidic water oxidation by dynamic migration of oxygen species at the Ir/Nb_2O_{5-x} catalyst/support interfaces. *Angew. Chem. Int. Ed.* **61**, e202212341 (2022).

23. Cheng, F. et al. Synergistic action of Co-Fe layered double hydroxide electrocatalyst and multiple ions of sea salt for efficient seawater oxidation at near-neutral pH. *Electrochim. Acta* **251**, 336–343 (2017).

24. Kuai, C. et al. Phase segregation reversibility in mixed-metal hydroxide water oxidation catalysts. *Nat. Catal.* **3**, 743–753 (2020).

25. Liu, E. et al. Unifying the hydrogen evolution and oxidation reactions kinetics in base by identifying the catalytic roles of hydroxyl-water-cation adducts. *J. Am. Chem. Soc.* **141**, 3232–3239 (2019).

26. Alexander, A.-M. & Hargreaves, J. S. J. Alternative catalytic materi-als: carbides, nitrides, phosphides and amorphous boron alloys. *Chem. Soc. Rev.* **39**, 4388–4401 (2010).

27. Niewa, R. & DiSalvo, F. J. Recent developments in nitride chemistry. *Chem. Mater.* **10**, 2733–2752 (1998).

28. Zhang, X.-L. et al. Plasma-assisted synthesis of metal nitrides for an efficient platinum-group-metal-free anion-exchange-membrane fuel cell. *Nano Lett.* **23**, 107–115 (2023).

29. Wang, Z. et al. Catalyst preparation with plasmas: how does it work? *ACS Catal.* **8**, 2093–2110 (2018).

30. Shebanova, O., Soignard, E. & McMillan, P. F. Compressibilities and phonon spectra of high-hardness transition metal-nitride materials. *High Press. Res.* **26**, 87–97 (2006).

31. Liu, H.-X. et al. Ptn–Ov synergistic sites on $MoOx/γ-Mo_2N$ hetero-structure for low-temperature reverse water–gas shift reaction. *Nat. Commun.* **13**, 5800 (2022).

32. Li, P. et al. Hydrogen bond network connectivity in the electric double layer dominates the kinetic pH effect in hydrogen electro-catalysis on Pt. *Nat. Catal.* **5**, 900–911 (2022).

33. Huang, B. et al. Cation- and pH-dependent hydrogen evolution and oxidation reaction kinetics. *JACS Au* **1**, 1674–1687 (2021).

34. Ataka, K., Yotsuyanagi, T. & Osawa, M. Potential-dependent reor-ientation of water molecules at an electrode/electrolyte interface studied by surface-enhanced infrared absorption spectroscopy. *J. Phys. Chem.* **100**, 10664–10672 (1996).

35. Pankewitz, T., Lagutschenkov, A., Niedner-Schatteburg, G., Xan-theas, S. S. & Lee, Y. T. Infrared spectrum of $NH_4^+(H_2O)$: evidence for mode specific fragmentation. *J. Chem. Phys.* **126**, 074307 (2007).

36. Grimaud, A. et al. Activating lattice oxygen redox reactions in metal oxides to catalyse oxygen evolution. *Nat. Chem.* **9**, 457–465 (2017).

37. Peng, J. et al. Design principles for transition metal nitride stability and ammonia generation in acid. *Joule* **7**, 150–167 (2023).

38. Alfarano, S. R. et al. Stripping away ion hydration shells in electrical double-layer formation: Water networks matter. *Proc. Natl. Acad. Sci. USA.* **118**, e2108568118 (2021).

39. Serva, A., Scalfi, L., Rotenberg, B. & Salanne, M. Effect of the metallicity on the capacitance of gold–aqueous sodium chloride interfaces. *J. Chem. Phys.* **155**, 044703 (2021).

40. Perra, D., Drenchev, N., Chakarova, K., Cutrufello, M. G. & Hadjii-vanov, K. Remarkable acid strength of ammonium ions in zeolites: FTIR study of low-temperature CO adsorption on NH_4FER. *RSC Adv.* **4**, 56183–56187 (2014).

41. de Lima, G. F., Duarte, H. A. & Pliego, J. R. Dynamical discrete/continuum linear response shells theory of solvation convergence test for NH_4^+ and OH^- ions in water solution using DFT and DFTB methods. *J. Phys. Chem. B* **114**, 15941–15947 (2010).

42. Li, J. et al. A fundamental viewpoint on the hydrogen spillover phenomenon of electrocatalytic hydrogen evolution. *Nat. Com-mun.* **12**, 3502 (2021).

43. Zhang, B. et al. A strongly coupled Ru–CrOx cluster–cluster het-erostructure for efficient alkaline hydrogen electrocatalysis. *Nat. Catal.* **7**, 441–451 (2024).

44. Yang, B., Huang, T., Dou, Y. & Kong, W. Stoichiometry ratio-induced structural and electronic properties changes of TaN thin films prepared by reactive magnetron sputtering. *Mater. Sci. Semicond. Proc.* **170**, 107979 (2024).

45. Lv, C. et al. Defect engineering metal-free polymeric carbon nitride electrocatalyst for effective nitrogen fixation under ambient con-ditions. *Angew. Chem. Int. Ed.* **57**, 10246–10250 (2018).

46. Yokoyama, Y. et al. In situ local pH measurements with hydrated iridium oxide ring electrodes in neutral pH aqueous solutions. *Chem. Lett.* **49**, 195–198 (2020).

47. Khatun, S. et al. New age chloride shielding strategies for corrosion resistant direct seawater splitting. *Chem. Commun.* **59**, 4578–4599 (2023).

48. Zhang, L., Jie, X., Shao, Z.-G., Wang, X. & Yi, B. The dynamic-state effects of sodium ion contamination on the solid polymer electro-lyte water electrolysis. *J. Power Sources* **241**, 341–348 (2013).

49. Bender, G. & Dinh, H. N. *National Renewable Energy Lab.(N-REL)* (2020).

50. Kresse, G. & Hafner, J. Ab initiomolecular dynamics for liquid metals. *Phys. Rev. B* **47**, 558–561 (1993).
51. Perdew, J. P., Burke, K. & Ernzerhof, M. Generalized gradient approximation made simple. *Phys. Rev. Lett.* **77**, 3865 (1996).
52. Blöchl, P. E. Projector augmented-wave method. *Phys. Rev. B* **50**, 17953–17979 (1994).
53. McCrory, C. C. L., Jung, S., Peters, J. C. & Jaramillo, T. F. Benchmarking heterogeneous electrocatalysts for the oxygen evolution reaction. *J. Am. Chem. Soc.* **135**, 16977–16987 (2013).

Acknowledgements

Author contributions

M.-R.G. supervised the project. X.-L.Z. and Y.-R.Z. performed the experiments, collected and analyzed the data. L.S. performed the HRTEM measurements. P.-C.Y. and S.-P.S. performed the SEM measurements. P.-P.Y., L.-P.C., and Z.-Z.W. helped with electrochemical data collection and analysis. M.-R.G. and X.-L.Z. co-wrote the manuscript. All authors discussed the results and commented on the manuscript. All authors discussed the results and commented on the manuscript.

Competing interests

The authors declare no competing interests.

Additional information

Supplementary information The online version contains supplementary material available at https://doi.org/10.1038/s41467-024-53724-1.

Correspondence and requests for materials should be addressed to Ya-Rong Zheng or Min-Rui Gao.

Peer review information *Nature Communications* thanks the anonymous reviewer(s) for their contribution to the peer review of this work. A peer review file is available.

Reprints and permissions information is available at http://www.nature.com/reprints

Publisher's note Springer Nature remains neutral with regard to jurisdictional claims in published maps and institutional affiliations.